Topological Kondo device for distinguishing quasi-Majorana and Majorana signatures

Donghao Liu,[1] Zhan Cao,[2] Xin Liu,[3] Hao Zhang,[1,2,4] and Dong E. Liu[1,2,4,*]

[1]*Department of Physics, State Key Laboratory of Low Dimensional Quantum Physics, Tsinghua University, Beijing 100084, China*

[2]*Beijing Academy of Quantum Information Sciences, Beijing 100193, China*

[3]*School of Physics and Wuhan National High Magnetic Field Center, Huazhong University of Science and Technology, Wuhan, Hubei 430074, China*

[4]*Frontier Science Center for Quantum Information, Beijing 100184, China*

(Received 16 December 2020; revised 16 September 2021; accepted 2 November 2021; published 22 November 2021)

To confirm the Majorana signatures, significant effort has been devoted to distinguishing between Majorana zero modes (MZMs) and spatially separated quasi-Majorana modes (QMMs). Because both MZMs and QMMs cause a quantized zero-bias peak in the conductance measurement, their verification task is thought to be very difficult. Here, we proposed a simple device with a single nanowire where the device could develop clear evidence of the topological Kondo effect in the topologically trivial phase with four QMMs. On the other hand, in the topological superconducting phase with MZMs, the transport signatures are significantly different. Therefore, our scheme provides a simple way to distinguish Majorana and quasi-Majorana modes.

DOI: 10.1103/PhysRevB.104.205125

I. INTRODUCTION

The topological superconductors can host localized zero-energy excitations named "Majorana zero modes" (MZMs) [1,2]. Among many experimental searches for MZMs, the semiconductor nanowire in proximity to an *s*-wave superconductor [3–19] proved to be one of the most promising platforms to study non-Abelian braiding statistics [20–23] and topological quantum computation [23,24]. Usually, a quantized zero-bias peak in the tunneling spectroscopy was considered as a smoking gun signature for the MZMs [25]. However, many recent works have shown that individual near-zero-energy Andreev bound states (ABSs) can also cause a zero-bias conductance anomaly [26–41]. (Such near-zero-energy ABS was also studied recently in two-dimensional vortex systems [42]). If the potential near the nanowire's edge is smooth [26], this ABS decomposes into two almost decoupled Majoranas [35–37]. Because such states are in the topologically trivial phase, the two decomposed Majoranas are also called "quasi-Majorana modes" (QMMs) [37]. (In the following, we will use MZMs to refer to the Majorana zero modes in the topological phase, QMMs to refer to the quasi-Majorana modes in the topologically trivial phase, and Majorana to refer to both). In the tunneling spectroscopy experiments, only one of the two QMMs couples to the outside metallic lead, resulting in also a robust quantized zero-bias conductance peak [36,41]. Therefore, it is tough to distinguish between QMMs and real MZMs in the local quantum transport experiments [35,36,43].

With the rapid progress of the Majorana search in the past years, significant effort has been devoted to studying the topological Kondo effect (TKE) due to the topological degeneracy of MZMs [44–72]. Different from the Kondo effect [73] which arises from the coupling between conduction electrons and quantum spin with degenerate levels, TKE arises from the coupling between conduction electrons and the nonlocal quantum spin caused by the topological degeneracy of MZMs. Not only the topological degeneracy, but also the TKE can demonstrate the non-Fermi liquid (NFL) [74,75] behavior which is unstable and difficult to achieve in the conventional Kondo context. Such TKE in its minimal setup [44–46] consists of a floating topological superconducting island supporting four localized MZMs ($M_{tot} = 4$), three of which ($M = 3$) are tunnel coupled to three conducting leads, respectively. The main experimental phenomenon of TKE is that as the temperature decreases, the linear conductance will then saturate at a fractional value ($G = 2e^2/Mh$) [44]. Besides, we believe that the measurement of TKE could both provide strong evidence of coherence nature in Majorana devices (alternative methods, such as Majorana teleportation interferometer [76] and dissipative Majorana teleportation [43]) and a transport characterization scheme for Majorana qubits.

A single Majorana nanowire system with smooth potentials at both ends could host four QMMs, which satisfy the minimum requirements for TKE. Therefore, we would like to ask if the TKE can be realized and observed experimentally in such a single-nanowire setup. In this paper, we propose a simple quasi-Majorana device with a single nanowire as shown in Fig. 1 to realize TKE in the topologically trivial phase and derive the conditions under which TKE could appear and potentially be observed in experiments. We believe that our device is much easier to realize for experimentalists than the standard TKE devices that require, at least, two nanowires. Besides, our device provides a robust experimental scheme to distinguish between topological MZMs and nontopological QMMs.

*Corresponding author. dongeliu@mail.tsinghua.edu.cn

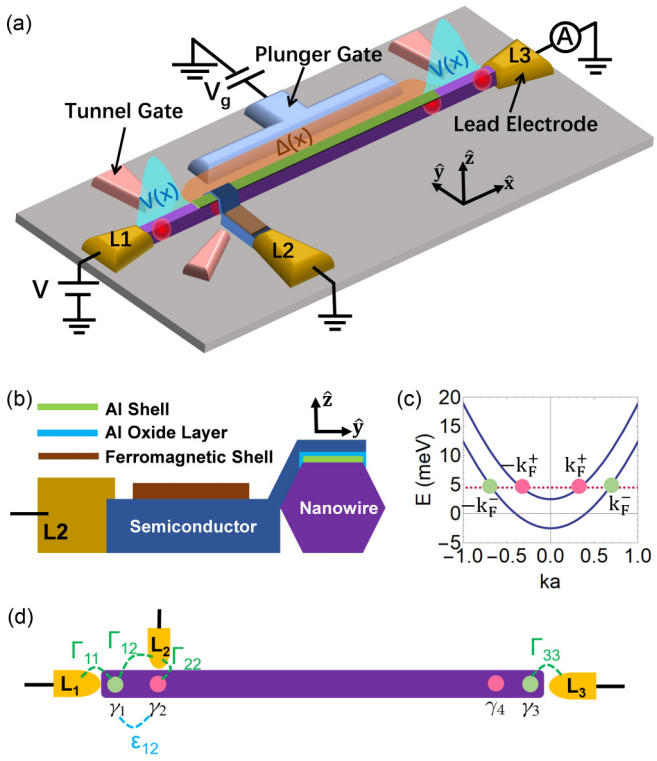

FIG. 1. (a) is the proposed experimental setup to study the TKE in quasi-Majorana nanowire. (b) is the cross-sectional view along with the tunneling probe to the lead $L2$ in (a). Here we consider a device structure similar to that in the experiment from Ref. [77] to detect the zero modes in the bulk of the wire. The semiconductor is also proximitized by the ferromagnetic shell (e.g., EuS) as the experimental devices shown in Refs. [78,79]. This magnetized part acts as a spin polarizer which allows only modes with a certain spin direction to strongly couple to the outside lead. (c) is the energy dispersion of a quasi-one-dimensional nanowire without the superconductor shell. (d) is a schematic of this three-lead setup. The most influential hybridizations are labeled.

II. PROPOSED DEVICE STRUCTURE

The proposed system setup is shown in Fig. 1(a). A semiconductor nanowire (purple) with Rashba spin-orbit coupling is in proximity to an s-wave superconductor shell (green). A magnetic-field B is applied in parallel with the nanowire. The nanowire is tunnel coupled to outside, so the central part including the nanowire and the superconductor shell forms a floating island. The floating island has finite Coulomb electrostatic energy which can be tuned by the plunger gate with voltage V_g. The tunnel gates control the couplings between the leads and the nanowire and give rise to the smooth potentials $V(x)$. The proximity-induced gap $\Delta(x)$ gradually vanishes in the regime where no superconducting shell is covered. Near the position where the superconductor shell vanished, a piece of semiconductor is in contact with the wire to detect the QMM in the bulk similar to the experimental device structure shown in Ref. [77]. The tunnel coupling between the nanowire and the semiconductor is achieved by applying a narrow tunnel gate or adding an insulating layer between them as performed in Ref. [77]. The semiconductor in proximity to a ferromagnetic shell shown in the T-shape leg in Fig. 1(a), and their cross-sectional view is shown in Fig. 1(b). The ferromagnetic insulator is used to magnetize the states in the semiconductor as those in recent experiments [78,79]. Each pair of QMMs at the same wire end always has the opposite spin polarization [37,80]. Therefore, the magnetized semiconductor near $L2$ further suppresses the potential "cross talk" between the quasi-Majorana mode at the end of the nanowire and the $L2$ lead. Besides lead $L2$, two more electrodes ($L1$, $L3$) cover the wire ends to detect the QMMs there. This three-leads setup is schematically shown in Fig. 1(d).

III. THE TKE IN THE QUASI-MAJORANA WIRE

A. Quasi-Majorana modes in a one-dimensional wire

Here will demonstrate that four QMMs could be generated in a single nanowire with smooth potentials at both sides [26,35–37]. The one-dimensional Bogoliubov–de Gennes (BdG) Hamiltonian of a Majorana nanowire extending in the x direction can be written as $\mathcal{H}_{\rm NW} = \frac{1}{2}\int dx\, \Psi^\dagger(x) H_{\rm NW} \Psi(x)$ with

$$H_{\rm NW} = \left(\frac{p_x^2}{2m^*} - \mu + V(x)\right)\sigma_0 \otimes \tau_z + \frac{\alpha}{\hbar} p_x \sigma_y \otimes \tau_z + V_{\rm Z}\sigma_x \otimes \tau_0 + \Delta(x)\sigma_0 \otimes \tau_x, \quad (1)$$

where $\Psi(x) = [\psi_\uparrow(x), \psi_\downarrow(x), \psi_\downarrow^\dagger(x), -\psi_\uparrow^\dagger(x)]^T$, $p_x = -i\hbar\partial_x$ is the momentum, m^* is the effective mass, μ is the chemical potential, V is the electrostatic potential, α is the spin-orbit coupling (SOC) strength, $V_{\rm Z}$ is the Zeeman energy due to the magnetic field parallel to the nanowire in the $-x$ direction, and Δ is the proximity-induced superconducting gap. σ_i and τ_i ($i = x, y, z$) are Pauli matrices which act on spin and particle-hole space, respectively. σ_0 and τ_0 are the corresponding identity matrices. Here we use a Gaussian shape $V(x) = V_0 \exp[(x - x_V)^2/\sigma_V^2]$ to model the smooth potential for both left and right junctions [see Figs. 1(a) and 2(b)]. The transition between the superconducting and the nonsuperconducting regimes is also smooth: $\Delta(x) = \Delta_0\{1 + \tanh[(x - x_\Delta)/\sigma_\Delta]\}$.

By discretizing the Hamiltonian (1) to a tight-binding model and solving it, we can obtain the spectrum and the wave functions of the QMMs and MZMs. The energy spectrums as a function of the Zeeman energy and chemical potential of this system are shown in Fig. 2(a) from which we can see there are zero modes both before and after the topological phase transition point ($V_{\rm Z}^2 = \mu^2 + \Delta_0^2$). MZMs appear in the topological regime ($V_{\rm Z} > V_{\rm Z}^c$ or $\mu < \mu^c$). In the topologically trivial regime there are two ABSs stuck to zero energy which are shown by two pairs of particle-hole symmetric zero-energy spectra before the phase transition point ($V_{\rm Z}^c$ or μ^c) in Fig. 2(a). Because in our case the potential variations at the left and right ends are identical, the two near-zero-energy ABSs are degenerate, and their spectra overlap with each other. The two ABSs can be decomposed into four QMMs, and their wave functions are shown in Fig. 2(c). For one ABS, its two particle-hole-symmetry-related BdG eigenstates are used to construct two Majorana wave-functions $\chi_A(x)$ and $\chi_B(x)$: $\chi_A = 1/\sqrt{2}(\varphi_{+\varepsilon}e^{i\theta} + \varphi_{-\varepsilon}e^{-i\theta})$, $\chi_B = i/\sqrt{2}(\varphi_{+\epsilon}e^{i\theta} - \varphi_{-\epsilon}e^{-i\theta})$, where $\varphi_{\pm\varepsilon}(x)$ are two eigenstate wave functions with near-zero eigenenergy $\pm\varepsilon$ and $\varphi_{-\epsilon} = P\varphi_{+\epsilon}$. P is the particle-hole symmetry operator with $P = (\sigma_y \otimes \tau_y)K$, where

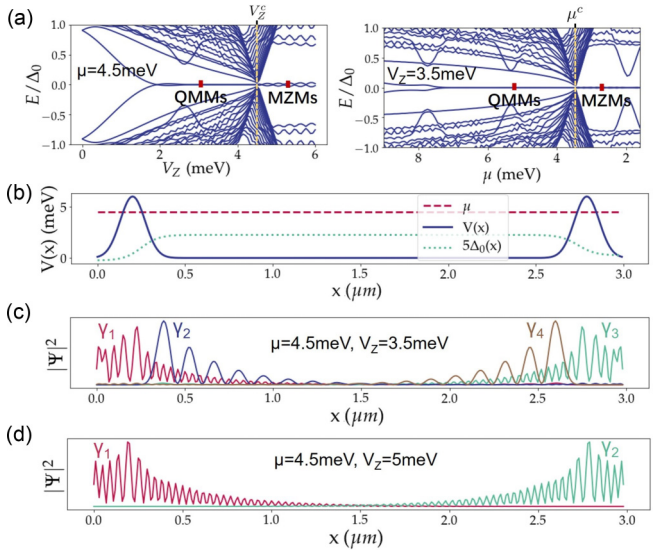

FIG. 2. (a) The energy spectrum of a bare quasi-Majorana nanowire with smooth potential on one side as a function of the Zeeman energy V_Z and the chemical potential μ. The critical V_Z^c ($\sqrt{\mu^2+\Delta_0^2}$) and μ^c ($\sqrt{V_Z^2-\Delta_0^2}$) at which topological phase transition happens are labeled. (b) The spatial distribution of the potential $V(x)$ and induced gap $\Delta(x)$. The parameters for the variation of the potential and the superconducting gap are $V_0 = 6$ meV, $x_V = 200$, $\sigma_V = 100$, $x_\Delta = 250$, and $\sigma_\Delta = 100$ nm. (c) The wave functions of four QMMs along the nanowire when $V_Z < V_Z^c$. (d) The wave functions of two MZMs in the topological regime when $V_Z > V_Z^c$. The other parameters of the nanowire are taken as: $m^* = 0.023m_e$, $\alpha = 50$ meV nm, the induced gap $\Delta_0 = 0.5$ meV, and the lattice constant $a = 10$ nm.

K is the complex conjugation. Then we can see that the wave-function $\chi_{\alpha\ (\alpha=A,B)}$ is particle-hole symmetric of itself. In the quasi-Majorana case, there is always a value of phase θ which will make χ_A and χ_B partially separated and only one of them located at the edge of the nanowire. If a lead is attached to the same edge, only one Majorana component will be detected by the outside and, therefore, in the tunneling experiment, the signatures will be the same as that of the topological Majorana. In a nanowire, two pairs of QMMs χ_A and χ_B can arise near the two wire ends as shown in Fig. 2(b). However, in the topological regime, there is only one pair of particle-hole-symmetric states remaining which corresponds to two Majorana states. The two Majorana wave functions are shown in Fig. 2(d).

B. The Bose condensate of the quasi-Majorana wire

Next we want to show that the quasi-Majorana wire can provide an effective Bose condensate and the QMMs-leads-coupled model can be mapped to the ideal TKE model [44]. The formation of quasi-Majoranas requires that the Fermi surface intersects two helical bands of the nanowire, forming two pairs of Fermi points as shown in Fig. 1(c). Although the system is in the topologically trivial regime if the scatterings between the two pairs of Fermi points $\pm k_F^+$ and $\pm k_F^-$ are weak enough (e.g., due to the smooth potential), the two bands can be seen as two independent spinless bands [26]. In the presence of the proximity-induced superconducting correlation, the proximity effect induces Cooper correlations for electrons near each pair of Fermi points and generates two Bose condensates. Each condensate bears two QMMs for which the spatial wave function is shown in Fig. 2(c). The inner two QMMs belong to one condensate, and the outer two QMMs belong to the other. Then with $M = 3$ leads coupled to three QMMs, the tunneling Hamiltonian can be written as

$$H_T = \sum_j t_{jj}\gamma_j\psi_j e^{i\phi_j/2} + \text{H.c.}, \tag{2}$$

where t_{jj} is the lead-QMM tunneling amplitude, ψ_j is the electron annihilation operator of lead-j ($j = 1$–3). $\phi_{1,3} = \phi_A$ and $\phi_{2,4} = \phi_B$ represent the phase of the outer (A) and inner (B) condensates. The operator $e^{\pm i\phi_j/2}$ in H_T increases or decreases the charge numbers in each condensate $[n_\alpha, e^{\pm i\phi_\alpha/2}] = \pm e^{\pm i\phi_\alpha/2}$, $\alpha = A, B$. Because the nanowire and the superconductor shell are floated, the Coulomb interactions between electrons will give rise to a Hamiltonian term $H_c(n) = E_c(n - n_g)^2$, where $n = n_A + n_B$ is the total electron number and E_c is the charging energy. The plunger gate controls the parameter n_g with $n_g = CV_g/e$, where C is the effective capacitance. Tuning n_g to an integer N, at an energy scale below E_c, the charge transfer between different leads is accompanied by virtual transitions connecting the lowest-energy charge state ($n = N$) of the island to the states with ± 1 extra electrons ($n = N \pm 1$). The physics is captured by the effective Hamiltonian,

$$H_{\text{eff}}^T = \sum_{j\neq k} \frac{t_{jj}t_{kk}^*}{E_c}\gamma_j\gamma_k\psi_k^\dagger\psi_j e^{i(\phi_j-\phi_k)/2}, \tag{3}$$

which is obtained by a Schrieffer-Wolf transformation [44,81] with $t_{jj} \ll E_c$. If γ_j and γ_k belong to different condensates there is phase exponential factor $e^{\pm i(\phi_A-\phi_B)/2}$ which represents the electron transfer between the two condensates. For our quasi-Majorana device, both condensates exchange Cooper pairs with the proximity superconductor at the same spatial positions; and, therefore, the effective coherent Josephson coupling $H_J = -E_J\cos(\phi_A - \phi_B)$ between the two condensates could be very strong. For a large E_J, $\phi_A - \phi_B$ will be fixed at 0. In addition, the two condensates together share the same spatial locations and only feel a single constant charging energy. Then H_{eff}^T is reduced to the ideal topological Kondo model [44]. Here, we note that in order to observe the TKE in the Majorana double wire "H-shape" qubits [82,83] (the simplest device to realize four MZMs using topological wires), we need: (1) the Cooper pairs in different topological wires to feel the same charging energy, and (2) the Josephson coupling between the two different wires is very strong. Therefore, our proposal provides a more natural platform for the TKE.

C. Conditions for the TKE

Here we will review the conditions for experimental observation of the TKE in a floating Majorana island with N MZMs coupling to M ($\leqslant N$) different metallic leads. Two key points for the TKE are as follows: (1) the temperature range where the TKE can be observed and (2) the strength of the Majorana-lead hybridizations as well as the Majorana-Majorana hybridizations. The Kondo temperature

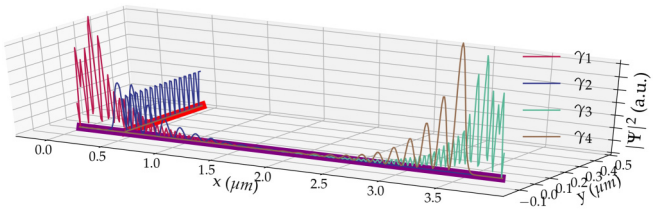

FIG. 3. The wave functions of the four QMMs γ_{1-4} when attaching the magnetized part. Relevant parameters are taken as $\mu = 4.5$ and $V_Z = 3.5$ meV. The length of the magnetized semiconductor is taken as 0.5 μm.

$T_K \simeq E_c \exp[-\pi E_c/2(M-2)\Gamma]$ describes the crossover energy scale between the trivial regime and the TKE regime, below which the typical NFL behavior of the TKE can be observed [44–46,81]. Γ is the average value of the Majorana level broadenings Γ_{jj} over all j leads with $\Gamma_{jj} = 2\pi\nu|t_{jj}|^2$ where ν is the density of states (DOS) at the Fermi level of the leads. However, in addition to the local couplings t_{jj} in Eq. (2), mutual couplings between MZMs and crossed couplings between γ_j and another lead k may also exist

$$H_M = i\sum_{j\neq k}\varepsilon_{jk}\gamma_j\gamma_k, \quad H_{T2} = \sum_{j\neq k} t_{jk}\gamma_j\psi_k e^{i\phi/2} + \text{H.c.}, \quad (4)$$

which are shown in Fig. 1(d). Here we name the ε_{jk}s Majorana-Majorana hybridizations, and $\Gamma_{jj} = 2\pi\nu|t_{jj}|^2$ and $\Gamma_{jk} = 2\pi\nu|t_{j\neq k}|^2$ local and nonlocal Majorana-lead hybridizations. The terms in Eq. (4) are relevant perturbations that can destroy the TKE. If these "imperfect terms" are small ($|t_{jk}|, \varepsilon_{jk} \ll t_{jj},\ j \neq k$), the TKEs could exist, but they give rise to another crossover energy scale T_h [49,53] below which these terms will drive the system away from the TKE regime of M MZMs to the TKE of $M-2$ MZMs. T_h can be estimated [49,53] as $T_h \simeq T_K(\bar{h}/T_K)^{M/2}$, where $\bar{h}$ is the typical value of the effective Majorana-Majorana hybridization: $\bar{h} = \max|h_{jk}| = \max|\varepsilon_{jk} + \sum_p \frac{t_{kp}t_{jp}^*}{iE_C}|$, which includes the effects from both two imperfect terms. For the case of $M = 3$, below T_h the system will be driven to a trivial state. This will result in a temperature window $T_h \ll T \ll T_K$ where the TKE can be observed. Hereafter we will call this window NFL window since in it the system is in a NFL state. The dependence of the size of this window $(T_K - T_h)/T_h$ on the Majorana-lead hybridization Γ and the Majorana-Majorana hybridization $\bar{h}$ is shown in Fig. 4(a) of Sec. (III E), which indicates that we have a large parameter regime to observe the TKE ($T_h \ll T_K$). The most satisfactory condition is that Γ is strong whereas is weak which means the three QMMs are independently coupled to the three leads, respectively.

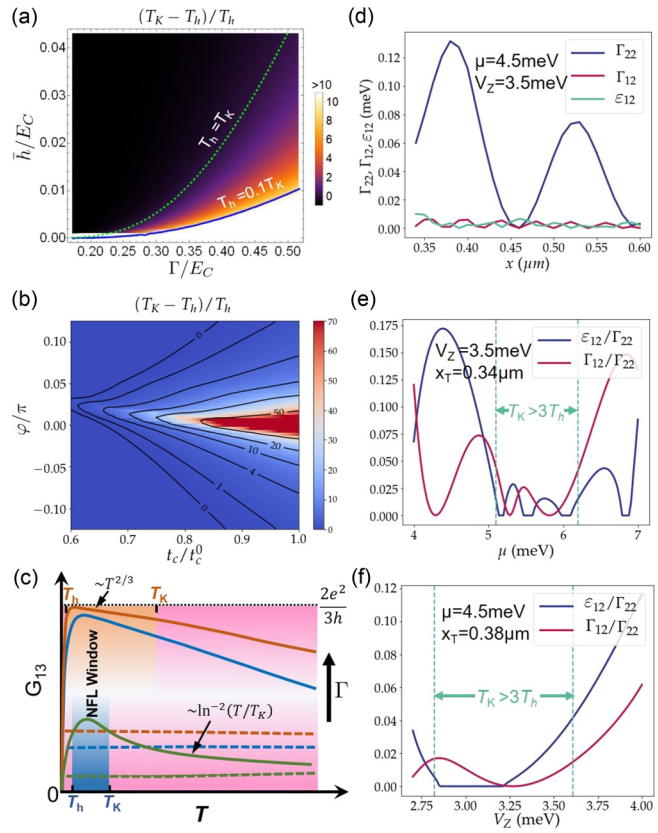

FIG. 4. (a) The relative size of the temperature window $(T_K - T_h)/T_h$ (in which TKE are allowed to be observed) as a function of the local Majorana-lead hybridization and the effective Majorana-Majorana hybridization. (b) The simulation result which gives the dependence of $(T_K - T_h)/T_h$ on the tunnel-coupling strength t_c/t_c^0 ($t_c^0 = 3$ meV) and the spin-polarization direction of the magnetized part. Relevant parameters used are $x_T = 0.38$ μm, $\mu = 4.5$, $V_Z = 3.2$, E_c MeV, and $\nu = 10$ meV^{-1}. (c) The conductance G_{13} for the setup shown in Fig. 1 as a function of temperature. The solid (dashed) lines describe the topological trivial case with QMMs (topological case with MZMs). The curves with the same local Majorana-lead hybridization Γ are drawn in the same color. The upper curves correspond to larger Γ (Γ is the average value of Γ_{jj}s). For the two upper solid curves which belong to the case of QMMs, their T_K and T_h are labeled with the same color as the corresponding curves. In the same manner, the blue (orange) shaded area indicates the NFL window of the blue (orange) solid curve. (d) The couplings Γ_{22}, Γ_{12}, and ε_{12} when the T leg is attached at different position x measured from the left side of the nanowire. (e) and (f) show ratios of the hybridization parameters Γ_{12}/Γ_{22} and $\varepsilon_{12}/\Gamma_{22}$ as a function of μ and V_Z. The range of μ and V_Z are chosen to support QMMs as shown in Fig. 2(a).

D. Attaching the T leg

Before studying the hybridizations when attaching the outside metallic leads, we first check whether the QMMs can be separated in order to satisfy the condition for the TKE. In a bare quasi-Majorana nanowire, the wave functions of four QMMs are shown in Fig. 2(c), and we saw the partially separated QMMs γ_1 and γ_2 (γ_3 and γ_4) located close to the left (right) end of the wire. At the left (right) end of the wire only the wave function of γ_1 (γ_3) has a distribution. Therefore, the lead $L1$ ($L3$) can only couple to γ_1 (γ_3) and the crossed Majorana-lead coupling between $L1$ and γ_2 ($L3$ and γ_4) can be neglected. Considering a long wire and a very smooth barrier potential landscape, we can imagine that the direct Majorana-Majorana coupling is very small. However, in the QMM nanowire, γ_1 and γ_2 are only partially separated in space, and there is some small but clearly visible contribution from γ_1 on top of the major γ_2 part as shown in Fig. 2(c). Therefore, both γ_1 and γ_2 could leak into the attached $L2$ lead

and cause strong crossed Majorana-lead couplings. Because the γ_1 and γ_2 have the opposite spin polarization [37,80], we consider adding a spin-polarized part to resolve this issue. As shown in Figs. 1(a) and 1(b), A T leg made of a ferromagnetically proximitized semiconductor is attached between the nanowire and the $L2$ lead. In order to reduce the effects, such as the induced local variation of the electrostatic potential, the contact between the T leg and the nanowire will be made narrow [84]. In our numerical simulation, the magnetization of this part is represented by the term $\boldsymbol{M}\cdot\boldsymbol{\sigma}$. The tunnel coupling between the nanowire and the magnetized semiconductor can be simulated by a small hopping term with hopping strength t_c [84,85]. When the spin polarization is at the $+x$ direction, the full spatial distributions of the quasi-Majorana wave functions are shown in Fig. 3. The numerical results tell us that the leakage from γ_1 into the T-leg $L2$ is very weak, and all the imperfect couplings with the $L2$ lead could be very small. Therefore, there could be a parameter interval that satisfies the TKE conditions. The details of the numerical calculation can be found in Appendix A.

E. The Majorana-Majorana and Majorana-lead hybridizations

Next, we calculate Majorana-Majorana hybridization ε_{ij} between γ_i and γ_j and Majorana-lead hybridizations $\Gamma_{ij} = 2\pi\nu|t_{ij}|^2$ between γ_i and lead Lj in order to quantitatively check whether our device can meet the condition for the TKE. Those hybridizations are labeled in Fig. 1(d). We have the situation that: (1) the wave functions of γ_1 and γ_2 have a finite small overlap, and (2) the attached magnetized T leg connects the wire in their overlapping regime and may disturb their hybridizations; and, therefore, the most influential hybridization factors are Γ_{12} and ε_{12}. Other hybridizations can be safely neglected. According to the expressions of T_{K} and T_{h}, we require small ratios Γ_{12}/Γ_{22} and $\varepsilon_{12}/\Gamma_{22}$ to reach the conditions, in general. We numerically compute those hybridizations in the lattice model using a kwant simulation [86]. We add the lead $L2$ to the end of the T leg and extract hybridization parameters from the single-terminal conductance. The details are shown in Appendix B.

The hybridization parameters are numerically shown in Figs. 4(d)–4(e). By changing the connection point x_{T} between the T leg and the nanowire from left to right, the coupling strengths oscillate as shown in Fig. 4(d). Those oscillations come from the variation of the wave functions and the spin densities of QMMs (shown in Appendix C). One can choose a range of x_{T} near γ_2 such that $\Gamma_{22} \gg \Gamma_{12}$ and ε_{12}, where the lead 2 is only strongly coupled to γ_2. In a practical situation with a fixed x_{T}, one can tune the value of Γ_{22}, Γ_{12}, and ε_{12} by shifting the wave function horizontally, which can be achieved by changing the chemical potential μ or the Zeeman energy V_{Z}. The ratios Γ_{12}/Γ_{22} and $\varepsilon_{12}/\Gamma_{22}$ as a function of μ and V_{Z} are plotted in Figs. 4(e) and 4(f), which indicates a large regime to observe the TKE. Besides, the lead-Majorana hybridizations are also related to the tunnel barrier. The dependence of the relative value $(T_{\mathrm{K}} - T_{\mathrm{h}})/T_{\mathrm{h}}$ on the coupling strength t_c among the nanowire, the magnetized semiconductor, and the magnetization direction angle φ is shown in Fig. 4(b). Here, the magnetization direction is represented by the angle φ through $(\cos\varphi\hat{\boldsymbol{x}} + \sin\varphi\hat{\boldsymbol{z}})$. The numerical result indicates a large parameter regime to support the TKE.

IV. QUASI-MAJORANA VS MAJORANA

Finally, we discuss how to distinguish the Majorana modes from the quasi-Majorana modes in our proposed setup shown in Fig. 1(a). In the experiment, one can apply a voltage on the $L1$ lead and detect the current in Lk lead ($k = 2, 3$), which yields the linear conductance $G_{1k} = \frac{dI_k}{dV_1}|_{V_1\to 0}$. By reducing the temperature much lower than E_c, G_{1k} will show Coulomb blockade (CB) oscillations: when the floating island is further away from the degenerate point where the electromagnetic energy of N and $N+1$ electrons are the same, the injected electron will be blockaded because of the large charging energy. By tuning n_g through the plunger gate, G_{1k} will alternately show peaks at the degenerate points $n_g = N + 1/2$ and valleys at $n_g = N$. In order to observe the TKE, n_g should be fixed at a value in the CB valley. In the CB valley when $T \ll E_c$, the noncoherent transport contributed by thermal excitations (the sequential tunneling process [66,72]) will be exponentially ($\sim e^{-E_c/T}$) suppressed [66,72]. The coherent transport signatures will help us to distinguish the QMMs and MZMs. Next we will discuss how to distinguish the two in the TKE temperature region.

If the nanowire is in the topologically trivial phase with four QMMs, the system will show the clear TKE as discussed before. When the temperature is lowered close to the Kondo temperature T_{K}, the electron transports are significantly modified by the Kondo physics, and the conductance G_{1k} will show the Kondo enhancement and a significant increase in the conductance will be observed. Further lowering the temperature below T_{K}, the strong correlations in the TKE regime will drive the couplings with three leads to the isotropic strong limit: $\Gamma_{jj}/\Gamma_{kk} \to 1$. The conductance will reach the fractional quantized value in a power-law way: $2e^2/3h - G_{1k} \propto T^{2/3}$ [44]. This convergence to $2e^2/3h$ and power-law dependence are NFL behaviors. However, when the temperature reaches $T \sim T_{\mathrm{h}}$, the coupling between γ_1 and γ_2 cannot be neglected anymore and the system will be driven out of the TKE regime as discussed in Sec. III C. The conductance will drop to 0 when T decreases. The above-mentioned behaviors of G_{13} are shown by the solid curves with large Γ in Fig. 4(c). The behavior of G_{12} is the same as that of G_{12} when $T > T_{\mathrm{h}}$, but at $T \ll T_{\mathrm{h}}$, G_{12} can still have a remaining value which is contributed by the local state formed by γ_1 and γ_2.

If the nanowire is in the topological phase, there are only two MZMs (γ_1 and γ_2) located at each side of the nanowire. Then, MZM γ_1 couples to both the $L1$ and the $L2$ leads, and MZM γ_2 couples to the $L3$ lead. In the CB valley, at low-temperature $T \ll E_c$, the conductance will be dominated by the cotunneling process between every two leads. Other higher-order processes involving the third lead will be suppressed by the large E_c. Then the conductance in the real Majorana case can be given by the two-terminal cotunneling results [87,88]: $G_{1k}^M \sim (e^2/h)\Gamma_1\Gamma_k/E_c^2$, where $\Gamma_{j(j=1-3)}$ is the hybridization between lead j and its nearest Majorana. Because the three Γ_js may not be equal, G_{12}^M and G_{13}^M are not necessarily equal. We demonstrate the low-temperature G_{13}^M

for the case that the three leads are symmetrically coupled to the nanowire in Fig. 4(c) using dashed lines where the upper dashed line indicates the case with larger Γ. In this case G_{12}^M is the same as G_{13}^M. There is no conductance enhancement due to the TKE.

Therefore, the QMMs can be distinguished from the MZMs by the conductance measurement featured the Kondo enhancement, as shown by the NFL window shown in Fig. 4(c). The fractional quantized conductance $G_{1k} = 2e^2/3h$ (also the $T^{2/3}$ law behavior towards it) will show the evidence of the TKE of QMMs. However, it is favorable to detect the nonlocal conductance G_{13} (or both G_{13} and G_{12}) instead of G_{12}. Because the leads $L1$ and $L2$ are very near to each other, it is more susceptible to the influence of local states. In the case that a quantum dot forms at the left end of the nanowire because of the potential variation, a real Majorana can leak into the dot and cause special conductance signals of a two-terminal detection. It is shown that due to the Majorana leakage to a side-coupled quantum dot and the conventional Kondo effect at the same time, the conductance between two leads connected to the quantum dot can be $e^2/2h$ (or $3e^2/2$ when there is an additional conventional Kondo conductance through the dot) at low temperature [89–91]. Although the conductance is not the characteristic fraction $2e^2/3h$ of TKE, a conductance enhancement may be observed in the real Majorana case and may mislead people. In contrast, the nonlocal conductance G_{13} only has the Kondo enhancement in the quasi-Majorana case. At last, the TKE can be further verified by the smoking gun signature: TKE should disappear if any one of the three leads is decoupled. For example, after decoupling the lead $L2$, the enhancement of conductance G_{13} will disappear. It is also worth mentioning, that with the larger hybridization strength Γ, this window can be easier to observe. When Γ is small, the temperature window between $T_{\rm h}$ and $T_{\rm K}$ will be small, and the quantized conductance will be hard to observe, but a conductance enhancement may also be observed as long as there is TKE physics as shown by the solid green curve in Fig. 4(c). In this case a logarithmic dependence $\sim \ln^{-2}(T/T_{\rm K})$ [44] on T when $T > T_{\rm K}$ can be taken as the evidence for the TKE.

V. CONCLUSIONS

In this paper, we proposed a simple experimental setup for observing the topological Kondo effect in a single nanowire system. In the topologically trivial phase, the nanowire can have four quasi-Majorana modes which share many same properties with the true Majorana modes but are protected by the smooth potential. We add three leads to the nanowire with two leads coupling the QMMs at the ends of the wire and one lead coupling the QMM in the bulk. (We also add a magnetized semiconductor to the latter one to suppress the unwanted crossed couplings). We study the conditions for observing the TKE and show that in this quasi-Majorana nanowire and found that when three quasi Majoranas strongly coupled to three leads topological Kondo effect could appear. At last, we show that our scheme could be applied to distinguish Majorana from quasi-Majorana systems through the transport signatures of the TKE in our proposed three-terminal device.

ACKNOWLEDGMENTS

We acknowledge support from Tsinghua University Initiative Scientific Research Program, NSF-China (Grants No. 11974198, No. 12004040), and the startup Grant from State Key Laboratory of Low-Dimensional Quantum Physics and Tsinghua University.

APPENDIX A: DETAILS OF THE SETUP OF QUASI-MAJORANA NANOWIRE

The Hamiltonian of the nanowire proximitized by the superconductor shown in Eq. (1) of the main text can be discretized on a one-dimensional atom chain,

$$\mathcal{H}_{\rm NW} = \frac{1}{2}\sum_i (\Psi_i^\dagger \{[2t - \mu + V(i)]\sigma_0 \otimes \tau_z + V_{\rm Z}\sigma_x \otimes \tau_0 + \Delta(i)\sigma_0 \otimes \tau_x\}\Psi_i - [\Psi_{i+a}^\dagger (t\sigma_0 + i\tilde{\alpha}\sigma_y) \otimes \tau_z \Psi_i + \text{H.c.}]), \tag{A1}$$

The Nambu spinor basis now is changed to $\Psi_i = (\psi_{i,\uparrow}, \psi_{i,\downarrow}, \psi_{i,\downarrow}^\dagger, -\psi_{i,\uparrow}^\dagger)^T$, where i labels the atom site and $i + a$ labels its nearest neighbor to the right. The hopping constant $t = \hbar^2/2m^*a^2 \approx 13$ meV and the Rashba SOC strength $\tilde{\alpha} = \alpha/2a = 2.5$ meV. The values of all the parameters can be found in the caption of Fig. 2 of the main text. $V(i)$ and $\Delta(i)$ are the discretizations of the potential $V(x)$ and the induced gap $\Delta(x)$ given in the main text and their the spatial distribution is shown in Fig. 2(b). Solving Eq. (A1) of a 3 μm wire gives the spectrum and the wave functions of the QMMs and MZMs as shown in Fig. 2. The eigenstate of Eq. (A1) can be written in a four-component vector form $(u_i, v_i)^T$, where u_i and v_i are the particle and the hole parts, respectively, and each has two spin components. The Majorana wave functions can be constructed with the particle-hole pair of near-zero-energy eigenstates $\varphi_\pm$,

$$\begin{bmatrix}\chi_A \\ \chi_B\end{bmatrix} = \frac{1}{\sqrt{2}}\begin{bmatrix}e^{i\theta} & e^{-i\theta} \\ ie^{i\theta} & -ie^{-i\theta}\end{bmatrix}\begin{bmatrix}\varphi_+ \\ \varphi_-\end{bmatrix}, \tag{A2}$$

where $\varphi_-(i) = P\varphi_+(i)$ and the particle-hole operator is $P = (\sigma_y \otimes \tau_y)K$. The Majorana wave-function $\chi_{\alpha\ (\alpha=A,Bt)}$ is self-particle-hole symmetric and, therefore, can be written as $\chi_\alpha = (\tilde{u}_{\alpha,i}, i\sigma_y\tilde{u}_{\alpha,i}^*)^T$, where $\tilde{u}_{\alpha,i} = (\tilde{u}_{\alpha,i\uparrow}, \tilde{u}_{\alpha,i\downarrow})$ is a two-component spinor. The phase θ in Eq. (1) is arbitrary which is not a physical phase. With each value of θ, through the unitary transformation in Eq. (1) one can obtain the wave functions of the two Majorana components. In the quasi-Majorana regime, there is always a value of θ which can make the two Majorana wave functions partially separated, and only one can be detected by the detector at the wire end. In this case we call the two Majorana components QMMs. Then for a single quasi-Majorana nanowire, when attaching a lead electrode to the wire end, only one QMM can strongly couple to the lead. Then the resulting tunneling conductance is $G(E) \approx (2e^2/h)[\Gamma^2/(E^2 + \Gamma^2)]$ which is same to that of topological MZMs. Therefore, it is hard to distinguish between MZMs and QMMs in a single-terminal tunneling experiment.

Next we talk about modeling of the T leg shown in Figs. 1(a) and 1(b). The tight-binding Hamiltonian of the magnetized semiconductor which is tunnel coupled to the

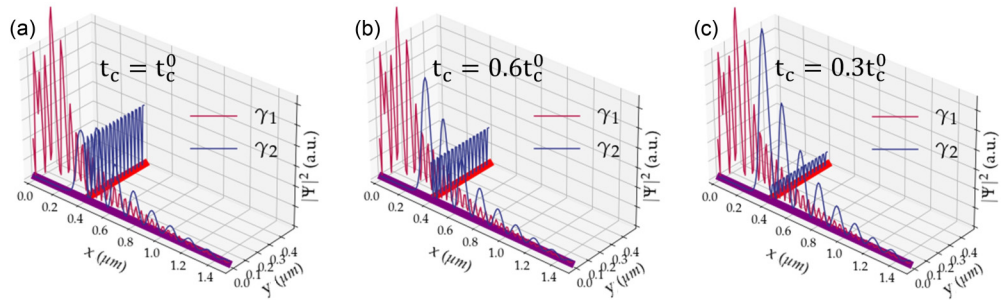

FIG. 5. The wave functions of the two QMMs $\gamma_{1,2}$ when attaching the semiconductor. (a)–(c) are the cases corresponding to $t_c = t_c^0, 0.6t_c^0, 0.3t_c^0$ with $t_c^0 = 3$ meV. The leakage of γ_2 to the T leg is suppressed when the tunneling barrier is high (small t_c). The parameters are taken as $\mu = 4.5$, $V_Z = 3.5$, $t_s = 3$, $\mu_s = 0$ meV, and $\boldsymbol{M} = M\hat{\boldsymbol{x}}$ with $M = 3$ meV. The length of the magnetized semiconductor is taken as 0.5 μm. The relatively smaller hopping t_s means that the semiconductor in the T leg has a relatively high DOS, which could make the coupling between γ_2 and lead $L2$ (when attached) stronger.

nanowire can be written as

$$\mathcal{H}_S = \frac{1}{2}\sum_j \{\Psi_j^\dagger[(2t_s - \mu_s)\sigma_0 \otimes \tau_z - \boldsymbol{M}\cdot\boldsymbol{\sigma}\otimes\tau_0]\Psi_j - [\Psi_{j+a_s}^\dagger(t_s\sigma_0\otimes\tau_z)\Psi_j + \text{H.c.}]\}, \tag{A3}$$

where j labels the lattice site and $j + a_s$ labels its nearest-neighbor site in the y direction, between the nearest sites between which the hopping constant is t_s. The term $\boldsymbol{M}\cdot\boldsymbol{\sigma}$ arises from the magnetization of this part. The chemical potential μ_s intersect the lower band split by $\boldsymbol{M}$ and the spin is polarized at the direction of $\boldsymbol{M}$. The direction can be written as $\boldsymbol{M} = M(\cos\varphi\hat{\boldsymbol{x}} + \sin\varphi\hat{\boldsymbol{z}})$. In the results of Figs. 3 and 4(d)–4(f) the magnetization is fixed at $+x$ with $\varphi = 0$. In Fig. 4(b), we allow the magnetization direction rotates on the x-z plane to study the dependence on φ.

The tunneled coupling between the nanowire and the semiconductor is described by the Hamiltonian $\mathcal{H}_{\text{hop}} = t_c\psi_i^\dagger\psi_j + \text{H.c.}$ Here site $i = \text{int}(x_T)$ is the position in the nanowire ($\mathcal{H}_{\text{NW}}$) where the T leg is attached and $j = 1$ is the end site of the magnetized semiconductor ($\mathcal{H}_S$). The quasi-Majorana wave functions of the cases corresponding to $t_c = t_c^0, 0.6t_c^0, 0.3t_c^0$ with $t_c^0 = 3$ meV are shown in Fig. 5. The leakage of the wave function of γ_2 to the T leg can be suppressed by lowering t_c. All relevant parameters are given in the caption. Figure 3 is in the same condition but with $t_c = 0.9t_c^0$. Figure 6 shows an alternative configuration to that of the main text shown in Fig. 1. Here a T-shape semiconductor nanowire is used. In experiments, this T-shape nanowire can be made through the epitaxial growth [92] or the selective area growth [93–95]. In order to polarize the spin, the T leg of the nanowire is covered by a ferromagnetic shell which can induce an exchange coupling in it. Here we reemphasize that the disturbance of the T leg to the nanowire should be minimized. Some works [84,96] studied the effects of the T leg on the bulk states of the nanowire and gave some solutions in the case of different configurations. This different proposed device may be valuable to experimentalists because it is made by different manufacturing processes. They can choose a simpler and easier-to-implement one according to the specific experimental conditions.

In the quasi-Majorana regime, the low-energy excitations of the hybrid device shown in Fig. 1(a) are QMMs. Their wave functions are shown in Fig. 3. Except for the four QMMs, all other states are above the superconducting gap and with their wave functions having very little distribution at the three end points of the device. Therefore, when leads are attached to each of the three end points, only the QMM near each end point has strong couplings with the lead attached there. Other states have very small couplings with the leads and are very hard to be excited at low temperatures. The only conducting channels in the central island are via the QMMs. If lead j has N_c channels, the couplings between all these channels and the Majorana γ_k can be expressed as

$$H_{T,jk} = N_c^{-1/2}\sum_{m=1}^{N_c} t_{jk}\gamma_k c_{mj}e^{i\phi/2} + \text{H.c.} \tag{A4}$$

Then the tunneling Hamiltonian between the leads and the device can be expressed as

$$H_{T,j} = \sum_k t_{jk}\gamma_k\psi_j e^{i\phi/2} + \text{H.c.}, \tag{A5}$$

where we have defined $\psi_j = N_c^{-1/2}\sum_{m=1}^{N_c} c_{mj}$. The N_c channels are equivalent to one effective channel. Here we have assumed that the leads are general metallic leads and all the

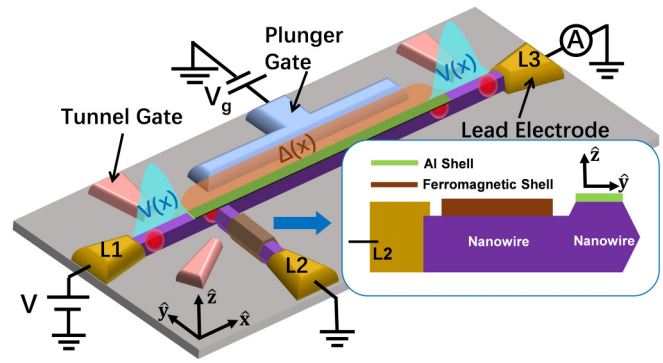

FIG. 6. An alternative setup to detect the TKE of QMMs for experimentalists. The T leg here is directly made by a T-shape nanowire. The T leg is covered by a ferromagnetic shell in order to polarize the spin. The theoretical models of this device and the one in Fig. 1 are the same, but the manufacturing difficulty of them may be different. Experimentalists can choose the easier-to-implement one.

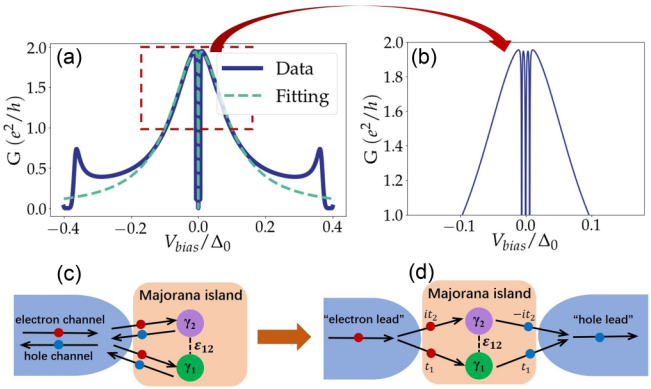

FIG. 7. (a) shows the single-terminal conductance (solid blue curve) detected by the L_2 lead and the fitting conductance (dashed green curve) using Eq. (B3) as a function of the bias voltage. (b) is a zoomed view of the simulated conductance peak in (a). The T leg is connected at $x_T = 0.42\ \mu$m from the left of the nanowire with $t_c = 0.83t_c^0$. $\mu_s = 2.5$ meV. The other parameters are the same as that of Fig. 5. (c) and (d) are schematics of a single-terminal tunneling process to detect Majorana. The electron and the hole channel in the lead have been divided into two virtual leads. As shown in (d), there are two paths from the "electron lead" to the "hole lead" which have interference with each other. In our case, the tunnelings between the lead and the two Majoranas have a $\pi/2$ phase difference (t_1 and it_2 where t_1 and t_2 are real). Then the accumulated phases of the two paths have a phase difference π as shown in (b) and, therefore, the interference of the two paths is in the most destructive case.

channels in each lead are equivalent (with the same coupling strength to each Majorana). The other complicated cases are beyond the scope of this paper, and it may be worthwhile to be studied elsewhere.

APPENDIX B: EVALUATING THE HYBRIDIZATION PARAMETERS FROM THE TUNNELING CONDUCTANCE

Here we will show the details about how we evaluate the Majorana-lead and Majorana-Majorana hybridization parameters when leads are attached to our device. As mentioned in the main text, the hybridization factors Γ_{12}, Γ_{22}, and ε_{12} are most influential and are simultaneously disturbed by the attached semiconductor. To evaluate these coupling parameters, we ground the nanowire, attach a normal metallic L_2 lead, and numerically compute the single-terminal tunneling conductance. Those parameters can then be extracted from those numerical results. Here, we assume that those hybridization couplings are the same even if we add a finite charging energy when considering a floating nanowire island. If the nanowire is sufficiently long, the hybridizations between the left QMMs $\gamma_{1,2}$ and the right QMMs $\gamma_{3,4}$ can be neglected. Under the Majorana basis, the effective Hamiltonian of two Majoranas on the left with finite hybridization ε_{12} is

$$H_{\text{eff}}^M = \begin{pmatrix} 0 & i\varepsilon_{12} \\ -i\varepsilon_{12} & 0 \end{pmatrix}, \tag{B1}$$

with the $L2$ lead attached to the end of the T leg, the effective coupling matrix between the lead and γ_1, γ_2 can be written as $W = \begin{pmatrix} \tau_{12} & -\tau_{12}^* \\ \tau_{22} & -\tau_{22}^* \end{pmatrix}$, where τ_{12}, τ_{22} are the effective couplings

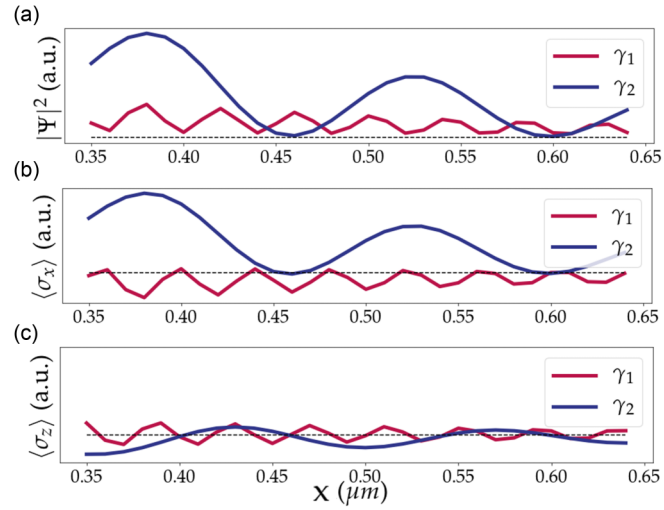

FIG. 8. The wave functions and the spin densities of the two QMMs γ_1 and γ_2. The ranges of the y axis of (a) and (b) are the same which shows that the spin is mainly in the $\pm x$ direction.

between L_2 lead and $\gamma_{1,2}$, and the two columns of the matrix W represent the electron part and the hole part of the L_2 lead, respectively. With the Mahaux-Weidenmüller formula we can obtain the scattering matrix of the junction between the device and the L_2 lead,

$$S(\omega) = 1 - 2\pi i W^\dagger \left(\omega - H_{\text{eff}}^M + i\pi W W^\dagger\right)^{-1} W. \tag{B2}$$

Then the single-terminal tunneling conductance in the L_2 lead when applying a bias voltage V ($V < \Delta_0$) is $G(V) = \frac{2e^2}{h} \text{Tr}\, S_{\text{he}}^\dagger\,(\text{eV}) S_{\text{he}}\,(\text{eV})$. Using Eq. (B2), we can obtain the conductance,

$$G(V) = \frac{2e^2}{h} \frac{(\Gamma_{12} - \Gamma_{22})^2\,(\text{eV})^2}{\left[(\text{eV})^2 - \varepsilon_{12}^2 - \Gamma_{12}\Gamma_{22}\right]^2 + (\Gamma_{12} + \Gamma_{22})^2\,(\text{eV})^2}, \tag{B3}$$

where $\Gamma_{ij} = 2\pi|\tau_{ij}|^2$ and τ_{12} and τ_{22} have a phase difference $\pi/2$. If the lead couples only one Majorana ($L2$ couples γ_2 in our case), the resonant Andreev reflection will result in a Lorentz-shaped conductance peak with maximum $2e^2/h$ as a function of bias voltage [25]. However, if another Majorana (γ_1) participates in the transport through the hybridization ε_{12} with γ_2 or the hybridization Γ_{21} with lead $L2$ will cause a splitting of the one Majorana peak. ε_{12} will couple γ_1 and γ_2 and move the energy of the state formed by them to $\pm\varepsilon_{12}$, and the resonant peak will be split. Γ_{21} will bring in another transport path through γ_1 which has a destructive interference with the path through γ_2 which can be seen in the virtual two-leads picture shown in Fig. 7(d). This process will also suppress the conductance and cause a dip at zero bias. The overall impact is included in Eq. (B3). Here Eq. (B3) is used to fit the result obtained from simulation of the tight-binding model given in Appendix A. As shown in Fig. 7(a), the blue curve in Fig. 7(a) is obtained from the KWANTsimulation [86], and the dashed green curve is fitted by Eq. (B3). The zoom view of the conductance peak shows that there is also a narrow split peak, which is contributed by the two QMMs on the

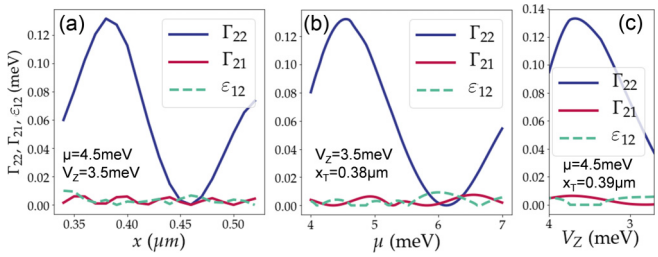

FIG. 9. The variations of hybridization parameters Γ_{22}, Γ_{12}, and ε_{12} as a function of x_T, μ, and V_Z.

other side of the nanowire. Nevertheless, their couplings to this lead are too weak, and we can neglect their influence. In Sec. (III E) of the main text, we assume that the nanowire is long enough, and we only consider the Majorana-Majorana and Majorana-lead hybridizations at the same end. The parameters used in Figs. 4(d)–4(f) are the same as that of Fig. 7.

APPENDIX C: WAVE FUNCTIONS AND SPIN DENSITIES OF QMMs

By changing the location x of the connection point of the L_2 lead, we can obtain a series of hybridization parameters with Eq. (B3) as shown in Fig. 4(d) of the main text. The spatial variations of Γ_{22} and Γ_{12} are related to the spatial distributions of the wave functions and spin densities of γ_1 and γ_2. Given the spinor representation of the particle-hole symmetric quasi-Majorana wave function $\chi_\alpha(i) = (\tilde{u}_{\alpha i\uparrow}, \tilde{u}_{\alpha i\downarrow}, \tilde{u}^*_{\alpha i\downarrow}, -\tilde{u}^*_{\alpha i\uparrow})^T$, the spin density of γ_α for different directions is obtained from the formula $\langle\sigma_\nu\rangle_\alpha(i) = \sum_{s,s'} u^*_{\alpha is}[\sigma_\nu]_{ss'}u_{\alpha is'}$. The amplitude of the wave functions and spin densities of γ_1 and γ_2 as a function of the position x in the same range of the connection point variation x_T of Fig. 4(d) is shown in Fig. 8. We can see that the two QMMs have opposite spin directions when projecting onto the σ_x eigenbasis. The two QMMs also have nonzero $\langle\sigma_z\rangle_\alpha$ which is much smaller than $\langle\sigma_x\rangle_\alpha$. The small $\langle\sigma_z\rangle_\alpha$ will result in a small asymmetry of the value of $(T_K - T_h)/T_h$ around $\varphi = 0$ shown in Fig. 4(b) of the main text.

With a fixed connection point x_T between the L_2 lead and the nanowire, the wave functions of QMMs can be shifted horizontally by changing the chemical potential of the nanowire μ or the Zeeman field V_Z; therefore, the hybridization can be tuned by changing μ and V_Z as well. A comparison of the hybridization couplings Γ_{22}, Γ_{12} and ε_{12} for changing the control parameters x_T, μ, V_Z is shown in Fig. 9. Therefore, in a practical situation with a fixed x_T, the values of hybridization parameters can be tuned by changing the chemical potential or the magnetic field.

[1] N. Read and D. Green, Phys. Rev. B **61**, 10267 (2000).
[2] A. Y. Kitaev, Phys.-Usp. **44**, 131 (2001).
[3] J. D. Sau, R. M. Lutchyn, S. Tewari, and S. Das Sarma, Phys. Rev. Lett. **104**, 040502 (2010).
[4] R. M. Lutchyn, J. D. Sau, and S. Das Sarma, Phys. Rev. Lett. **105**, 077001 (2010).
[5] Y. Oreg, G. Refael, and F. von Oppen, Phys. Rev. Lett. **105**, 177002 (2010).
[6] J. Alicea, Phys. Rev. B **81**, 125318 (2010).
[7] A. Cook and M. Franz, Phys. Rev. B **84**, 201105(R) (2011).
[8] J. Alicea, Rep. Prog. Phys. **75**, 076501 (2012).
[9] V. Mourik, K. Zuo, S. M. Frolov, S. R. Plissard, E. P. A. M. Bakkers, and L. P. Kouwenhoven, Science **336**, 1003 (2012).
[10] L. P. Rokhinson, X. Liu, and J. K. Furdyna, Nat. Phys. **8**, 795 (2012).
[11] M. T. Deng, C. L. Yu, G. Y. Huang, M. Larsson, P. Caroff, and H. Q. Xu, Nano Lett. **12**, 6414 (2012).
[12] A. Das, Y. Ronen, Y. Most, Y. Oreg, M. Heiblum, and H. Shtrikman, Nat. Phys. **8**, 887 (2012).
[13] H. O. H. Churchill, V. Fatemi, K. Grove-Rasmussen, M. T. Deng, P. Caroff, H. Q. Xu, and C. M. Marcus, Phys. Rev. B **87**, 241401(R) (2013).
[14] A. D. K. Finck, D. J. Van Harlingen, P. K. Mohseni, K. Jung, and X. Li, Phys. Rev. Lett. **110**, 126406 (2013).
[15] S. Nadj-Perge, I. K. Drozdov, J. Li, H. Chen, S. Jeon, J. Seo, A. H. MacDonald, B. A. Bernevig, and A. Yazdani, Science **346**, 602 (2014).
[16] S. M. Albrecht, A. P. Higginbotham, M. Madsen, F. Kuemmeth, J. Jespersen, T. S. Nygard, P. Krogstrup, and C. M. Marcus, Nature (London) **531**, 206 (2016).
[17] M. Deng, S. Vaitiekėnas, E. B. Hansen, J. Danon, M. Leijnse, K. Flensberg, J. Nygård, P. Krogstrup, and C. M. Marcus, Science **354**, 1557 (2016).
[18] H. Zhang, Ö. Gül, S. Conesa-Boj, M. Nowak, M. Wimmer, K. Zuo, V. Mourik, F. K. de Vries, J. van Veen, M. W. A. de Moor, J. D. S. Bommer, D. J. van Woerkom, D. Car, S. R. Plissard, E. P. A. M. Bakkers, M. Quintero-Pérez, M. C. Cassidy, S. Koelling, S. Goswami, K. Watanabe *et al.*, Nat. Commun. **8**, 16025 (2017).
[19] Ö. Gül, H. Zhang, J. D. S. Bommer, M. W. A. de Moor, D. Car, S. R. Plissard, E. P. A. M. Bakkers, A. Geresdi, K. Watanabe, T. Taniguchi, and L. P. Kouwenhoven, Nat. Nanotechnol. **13**, 192 (2018).
[20] J. M. Leinaas and J. Myrheim, Nuovo Cimento Soc. Ital. Fis., B **37**, 1 (1977).
[21] K. Fredenhagen, K. H. Rehren, and B. Schroer, Commun. Math. Phys. **125**, 201 (1989).
[22] D. A. Ivanov, Phys. Rev. Lett. **86**, 268 (2001).
[23] C. Nayak, S. H. Simon, A. Stern, M. Freedman, and S. Das Sarma, Rev. Mod. Phys. **80**, 1083 (2008).
[24] A. Kitaev, Ann. Phys. **303**, 2 (2002).
[25] K. T. Law, P. A. Lee, and T. K. Ng, Phys. Rev. Lett. **103**, 237001 (2009).
[26] G. Kells, D. Meidan, and P. W. Brouwer, Phys. Rev. B **86**, 100503(R) (2012).
[27] D. Roy, N. Bondyopadhaya, and S. Tewari, Phys. Rev. B **88**, 020502(R) (2013).
[28] J. Cayao, E. Prada, P. San-Jose, and R. Aguado, Phys. Rev. B **91**, 024514 (2015).
[29] J. Klinovaja and D. Loss, Eur. Phys. J. B **88**, 62 (2015).

[30] P. San-Jose, J. Cayao, E. Prada, and R. Aguado, Sci. Rep. **6**, 21427 (2016).

[31] C.-X. Liu, J. D. Sau, T. D. Stanescu, and S. Das Sarma, Phys. Rev. B **96**, 075161 (2017).

[32] F. Setiawan, C.-X. Liu, J. D. Sau, and S. Das Sarma, Phys. Rev. B **96**, 184520 (2017).

[33] F. Peñaranda, R. Aguado, P. San-Jose, and E. Prada, Phys. Rev. B **98**, 235406 (2018).

[34] C. Reeg, O. Dmytruk, D. Chevallier, D. Loss, and J. Klinovaja, Phys. Rev. B **98**, 245407 (2018).

[35] C. Moore, T. D. Stanescu, and S. Tewari, Phys. Rev. B **97**, 165302 (2018).

[36] C. Moore, C. Zeng, T. D. Stanescu, and S. Tewari, Phys. Rev. B **98**, 155314 (2018).

[37] A. Vuik, B. Nijholt, A. R. Akhmerov, and M. Wimmer, SciPost Phys. **7**, 061 (2019).

[38] O. A. Awoga, J. Cayao, and A. M. Black-Schaffer, Phys. Rev. Lett. **123**, 117001 (2019).

[39] Z. Cao, H. Zhang, H.-F. Lü, W.-X. He, H.-Z. Lu, and X.-C. Xie, Phys. Rev. Lett. **122**, 147701 (2019).

[40] H. Pan and S. Das Sarma, Phys. Rev. Research **2**, 013377 (2020).

[41] H. Pan, W. S. Cole, J. D. Sau, and S. Das Sarma, Phys. Rev. B **101**, 024506 (2020).

[42] O. Dmytruk, D. Loss, and J. Klinovaja, Phys. Rev. B **102**, 245431 (2020).

[43] D. Liu, Z. Cao, H. Zhang, and D. E. Liu, Phys. Rev. B **101**, 081406(R) (2020).

[44] B. Béri and N. R. Cooper, Phys. Rev. Lett. **109**, 156803 (2012).

[45] A. Altland and R. Egger, Phys. Rev. Lett. **110**, 196401 (2013).

[46] B. Béri, Phys. Rev. Lett. **110**, 216803 (2013).

[47] N. Crampé and A. Trombettoni, Nucl. Phys. B **871**, 526 (2013).

[48] A. M. Tsvelik, Phys. Rev. Lett. **110**, 147202 (2013).

[49] M. R. Galpin, A. K. Mitchell, J. Temaismithi, D. E. Logan, B. Béri, and N. R. Cooper, Phys. Rev. B **89**, 045143 (2014).

[50] A. Zazunov, A. Altland, and R. Egger, New J. Phys. **16**, 015010 (2014).

[51] A. M. Tsvelik, New J. Phys. **16**, 033003 (2014).

[52] A. Altland, B. Béri, R. Egger, and A. M. Tsvelik, J. Phys. A: Math. Theor. **47**, 265001 (2014).

[53] A. Altland, B. Béri, R. Egger, and A. M. Tsvelik, Phys. Rev. Lett. **113**, 076401 (2014).

[54] E. Eriksson, C. Mora, A. Zazunov, and R. Egger, Phys. Rev. Lett. **113**, 076404 (2014).

[55] E. Eriksson, A. Nava, C. Mora, and R. Egger, Phys. Rev. B **90**, 245417 (2014).

[56] O. Kashuba and C. Timm, Phys. Rev. Lett. **114**, 116801 (2015).

[57] F. Buccheri, H. Babujian, V. E. Korepin, P. Sodano, and A. Trombettoni, Nucl. Phys. B **896**, 52 (2015).

[58] S. Plugge, A. Zazunov, E. Eriksson, A. M. Tsvelik, and R. Egger, Phys. Rev. B **93**, 104524 (2016).

[59] L. Herviou, K. Le Hur, and C. Mora, Phys. Rev. B **94**, 235102 (2016).

[60] F. Buccheri, G. D. Bruce, A. Trombettoni, D. Cassettari, H. Babujian, V. E. Korepin, and P. Sodano, New J. Phys. **18**, 075012 (2016).

[61] D. Giuliano, P. Sodano, A. Tagliacozzo, and A. Trombettoni, Nucl. Phys. B **909**, 135 (2016).

[62] D. Giuliano, G. Campagnano, and A. Tagliacozzo, Eur. Phys. J. B **89**, 251 (2016).

[63] A. Zazunov, F. Buccheri, P. Sodano, and R. Egger, Phys. Rev. Lett. **118**, 057001 (2017).

[64] B. Béri, Phys. Rev. Lett. **119**, 027701 (2017).

[65] Z.-q. Bao and F. Zhang, Phys. Rev. Lett. **119**, 187701 (2017).

[66] K. Michaeli, L. A. Landau, E. Sela, and L. Fu, Phys. Rev. B **96**, 205403 (2017).

[67] L. A. Landau and E. Sela, Phys. Rev. B **95**, 035135 (2017).

[68] A. Latief and B. Béri, Phys. Rev. B **98**, 205427 (2018).

[69] K. Snizhko, F. Buccheri, R. Egger, and Y. Gefen, Phys. Rev. B **97**, 235139 (2018).

[70] M. Gau, S. Plugge, and R. Egger, Phys. Rev. B **97**, 184506 (2018).

[71] M. Papaj, Z. Zhu, and L. Fu, Phys. Rev. B **99**, 014512 (2019).

[72] J. I. Väyrynen, A. E. Feiguin, and R. M. Lutchyn, Phys. Rev. Research **2**, 043228 (2020).

[73] J. Kondo, Prog. Theor. Phys. **32**, 37 (1964).

[74] G. Stewart, Rev. Mod. Phys. **73**, 797 (2001).

[75] A. J. Schofield, Contemp. Phys. **40**, 95 (1999).

[76] L. Fu, Phys. Rev. Lett. **104**, 056402 (2010).

[77] A. Grivnin, E. Bor, M. Heiblum, Y. Oreg, and H. Shtrikman, Nat. Commun. **10**, 1940 (2019).

[78] S. Vaitiekėnas, Y. Liu, P. Krogstrup, and C. Marcus, Nat. Phys. **17**, 43 (2021).

[79] S. Manna, P. Wei, Y. Xie, K. T. Law, P. A. Lee, and J. S. Moodera, Proc. Natl. Acad. Sci. USA **117**, 8775 (2020).

[80] T. D. Stanescu and S. Tewari, Phys. Rev. B **100**, 155429 (2019).

[81] A. C. Hewson, *The Kondo Problem to Heavy Fermions* (Cambridge University Press, Cambridge, 1997).

[82] T. Karzig, C. Knapp, R. M. Lutchyn, P. Bonderson, M. B. Hastings, C. Nayak, J. Alicea, K. Flensberg, S. Plugge, Y. Oreg, C. M. Marcus, and M. H. Freedman, Phys. Rev. B **95**, 235305 (2017).

[83] H. Zhang, D. E. Liu, M. Wimmer, and L. P. Kouwenhoven, Nat. Commun. **10**, 5128 (2019).

[84] Y. Huang, J. D. Sau, T. D. Stanescu, and S. Das Sarma, Phys. Rev. B **98**, 224512 (2018).

[85] S. Das Sarma, A. Nag, and J. D. Sau, Phys. Rev. B **94**, 035143 (2016).

[86] C. W. Groth, M. Wimmer, A. R. Akhmerov, and X. Waintal, New J. Phys. **16**, 063065 (2014).

[87] R. Hützen, A. Zazunov, B. Braunecker, A. L. Yeyati, and R. Egger, Phys. Rev. Lett. **109**, 166403 (2012).

[88] J. Ekström, P. Recher, and T. L. Schmidt, Phys. Rev. B **101**, 195420 (2020).

[89] D. E. Liu and H. U. Baranger, Phys. Rev. B **84**, 201308(R) (2011).

[90] E. Vernek, P. H. Penteado, A. C. Seridonio, and J. C. Egues, Phys. Rev. B **89**, 165314 (2014).

[91] D. A. Ruiz-Tijerina, E. Vernek, L. G. G. V. DiasdaSilva, and J. C. Egues, Phys. Rev. B **91**, 115435 (2015).

[92] S. Gazibegovic, D. Car, H. Zhang, S. C. Balk, J. A. Logan, M. W. A. de Moor, M. C. Cassidy, R. Schmits, D. Xu, G. Wang, P. Krogstrup, R. L. M. Op het Veld, K. Zuo, Y. Vos, J. Shen, D. Bouman, B. Shojaei, D. Pennachio, J. S. Lee, P. J. van Veldhoven *et al.*, Nature (London) **548**, 434 (2017).

[93] F. Krizek, J. E. Sestoft, P. Aseev, S. Marti-Sanchez, S. Vaitiekėnas, L. Casparis, S. A. Khan, Y. Liu, T. Stankevič, A. M. Whiticar, A. Fursina, F. Boekhout, R. Koops, E. Uccelli, L. P. Kouwenhoven, C. M. Marcus, J. Arbiol, and P. Krogstrup, Phys. Rev. Mater. **2**, 093401 (2018).

[94] S. Vaitiekėnas, A. M. Whiticar, M.-T. Deng, F. Krizek, J. E. Sestoft, C. J. Palmstrøm, S. Marti-Sanchez, J. Arbiol, P. Krogstrup, L. Casparis, and C. M. Marcus, Phys. Rev. Lett. **121**, 147701 (2018).

[95] R. L. O. het Veld, D. Xu, V. Schaller, M. A. Verheijen, S. M. Peters, J. Jung, C. Tong, Q. Wang, M. W. de Moor, B. Hesselmann *et al.*, Commun. Phys. **3**, 59 (2020).

[96] T. D. Stanescu and S. Das Sarma, Phys. Rev. B **97**, 045410 (2018).